arXiv:astro-ph/0601498v1 23 Jan 2006

Rotating massive stars @ very low Z: high C & N production

Raphael HIRSCHI

Dept. of physics and Astronomy, University of Basel, Klingelbergstr. 82, 4056 Basel, Switzerland

Abstract. Two series of models and their yields are presented in this paper. The first series consists of 20 $M_\odot$ models with varying initial metallicity (solar down to $Z = 10^{-8}$) and rotation ($\upsilon_{\rm ini} = 0 - 600\,{\rm km\,s^{-1}}$). The second one consists of models with an initial metallicity of $Z = 10^{-8}$, masses between 20 and 85 $M_\odot$ and average rotation velocities at these metallicities ($\upsilon_{\rm ini} = 600 - 800\,{\rm km\,s^{-1}}$). The most interesting models are the models with $Z = 10^{-8}$ ([Fe/H]~ -6.6). In the course of helium burning, carbon and oxygen are mixed into the hydrogen burning shell. This boosts the importance of the shell and causes a reduction of the size of the CO core. Later in the evolution, the hydrogen shell deepens and produces large amount of primary nitrogen. For the most massive models ($M \gtrsim 60\,M_\odot$), significant mass loss occurs during the red supergiant stage. This mass loss is due to the surface enrichment in CNO elements via rotational and convective mixing.

The yields of the fast rotating 20 $M_\odot$ models can best reproduce (within our study) the observed abundances at the surface of extremely metal poor (EMP) stars. The wind of the massive models can reproduce the CNO abundances of the carbon–rich UMPs, in particular for the most metal poor star known to date, HE1327-2326.

Keywords: Stars: abundances – evolution – rotation – mass loss
PACS: 97.10.Cv

INTRODUCTION

Precise measurements of abundances of extremely metal poor (EMP) stars have recently been obtained by Cayrel et al. [1], Spite et al. [2], Israelian et al. [3], ... These provide new constraints for the stellar evolution models [see 4, 5, 6]. The most striking constraint is the need for primary ^{14}N production in very low metallicity massive stars. Other possible constraints are an upturn of the C/O ratio with a [C/Fe] about constant or slightly decreasing (with increasing metallicity) at very low metallicities, which requires an increase (with increasing metallicity) of oxygen yields below [Fe/H]$\sim$ -3. About one quarter of EMP stars are carbon rich (C-rich EMP, CEMP stars). Ryan et al. [7] propose a classification for these stars. They find two categories: about three quarter are main s-process enriched (Ba-rich) stars and one quarter are enriched with a weak component of s-process (Ba-normal). The two most metal poor stars known to date, HE1327-2326 [8, 9] and HE 0107-5240 [10] are both CEMP stars. These stars are believed to have been enriched by only one to several stars and we can therefore compare our yields to their observed abundances without the filter of a galactic chemical evolution model (GCE). In an attempt to explain the origin of the abundances observed as well as the metallicity trends, I computed pre-supernova evolution models of rotating single stars with metallicities ranging from solar metallicity down to $Z = 10^{-8}$ following the work of Meynet et al. [11].

DESCRIPTION OF THE STELLAR MODELS

The computer model used to calculate the stellar models is described in detail in Hirschi et al. [12]. At low metallicities the mixture of the heavy elements we adopted is the one used to compute the opacity tables for Weiss 95's alpha–enriched composition [13]. The mass loss rates are described and discussed in Meynet et al. [11]. Very little was known about the mass loss of very low metallicity stars with a strong enrichment in CNO elements until recently. Vink and de Koter [14] study the case of WR stars but a crucial case, which has not been studied in detail yet, is the case of red supergiant stars (RSG). As we shall see later, due to rotational and convective mixing, the surface of the star is strongly enriched in CNO elements during the RSG stage. Awaiting for future studies, it is implicitly assumed in this work (as in Meynet et al. [11]) that CNO elements have a significant contribution to opacities and mass loss rates. This assumption is supported by the possible formation of molecular lines in the RSG stage. Therefore the mass loss rates depend on metallicity as $\dot{M} \sim (Z/Z_{\odot})^{0.5}$, where Z is the mass fraction of heavy elements at the surface of the star. The evolution of the models was in general followed until core Si–burning and the stellar yields are calculated as in Hirschi et al. [15]. The main characteristics of the models are presented in Table 1. More details about the models are presented in Hirschi [16].

The value of 300 $\mathrm{km\,s^{-1}}$ used for the initial rotation velocity at solar metallicity corresponds to an average velocity of about 220 $\mathrm{km\,s^{-1}}$ on the Main Sequence (MS) which is very close to the average observed value [see for instance 17]. It is unfortunately not possible to measure the rotational velocity of very low metallicity massive stars since they all died a long time ago. Nevertheless, there is indirect evidence that stars with a lower metallicity have a higher rotation velocity. This can be due to the difficulty of evacuating angular momentum during the star formation, which is even more important at lower metallicities [see 18]. Furthermore, a very low metallicity star containing the same angular momentum as a solar metallicity star has a higher surface rotation velocity due to its smaller radius (one quarter of $Z_{\odot}$ radius for 20 $M_{\odot}$ stars). In order to compare the models at different metallicities and with different initial masses, the ratio $\upsilon_{\mathrm{ini}}/\upsilon_{\mathrm{crit}}$ is used (see Table 1). υ_{crit} is the critical velocity at which matter becomes gravitationally unbound. $\upsilon_{\mathrm{ini}}/\upsilon_{\mathrm{crit}}$ increases only as $r^{-1/2}$ for models with the same angular momentum (J) but lower metallicity, whereas the surface rotational velocity increases as r^{-1} ($J \sim \upsilon r$). The angular momentum can be compared as well but one has to bear in mind that it varies significantly for models of different initial masses. Finally, $\upsilon_{\mathrm{ini}}/\upsilon_{\mathrm{crit}}$ is a good indicator for the impact of rotation on mass loss.

In the first series of models, the aim is to scan the parameter space of rotation and metallicity with 20 $M_{\odot}$ models since a 20 $M_{\odot}$ star is not far from the average massive star concerning stellar yields. For this series, two initial rotational velocities were used at very low metallicities. The first one is the same as at solar metallicity, 300 $\mathrm{km\,s^{-1}}$. The second υ_{ini} is 500 at Z=10^{-5} ([Fe/H]$\sim$-3.6) and 600 $\mathrm{km\,s^{-1}}$ at Z=10^{-8} ([Fe/H]$\sim$-6.6). These second values have ratios of the initial velocity to the break–up velocity, $\upsilon_{\mathrm{ini}}/\upsilon_{\mathrm{crit}}$, around 0.55, which is only slightly larger than the solar metallicity value (0.44). The 20 $M_{\odot}$ model at Z=10^{-8} and with 600 $\mathrm{km\,s^{-1}}$ has a total initial angular momentum $J_{\mathrm{tot}} = 3.3\,10^{52}$ erg s which is the same as the solar metallicity 20 $M_{\odot}$ model

TABLE 1. Initial parameters of the models (columns 1–5): mass, metallicity, rotation velocity [km s^{-1}], total angular momentum [10^{53} erg s] and $\upsilon_{\rm ini}/\upsilon_{\rm crit}$. Total lifetime [Myr] and various masses [$M_\odot$] (7–10): final mass, masses of the helium and carbon–oxygen cores and the remnant mass. Total stellar yields (wind + SN) [$M_\odot$] for carbon (11), nitrogen (12) and oxygen (13).

$M_{\rm ini}$	$Z_{\rm ini}$	$\upsilon_{\rm ini}$	$J_{\rm tot}^{\rm ini}$	$\frac{\upsilon_{\rm ini}}{\upsilon_{\rm crit}}$	$\tau_{\rm life}$	$M_{\rm final}$	M_α	$M_{\rm CO}$	$M_{\rm rem}$	^{12}C	^{14}N	^{16}O
20	2e-02	300	0.36	0.44	11.0	8.763	8.66	6.59	2.57	0.433	4.33e-2	2.57
20	1e-03	000	–	0.00	10.0	19.557	6.58	4.39	2.01	0.373	3.31e-3	1.46
20	1e-03	300	0.34	0.39	11.5	17.190	8.32	6.24	2.48	0.676	3.10e-3	2.70
20	1e-05	000	–	0.00	9.80	19.980	6.24	4.28	1.98	0.370	4.27e-5	1.50
20	1e-05	300	0.27	0.34	11.1	19.930	7.90	5.68	2.34	0.481	1.51e-4	2.37
20	1e-05	500	0.42	0.57	11.6	19.575	7.85	5.91	2.39	0.648	5.31e-4	2.59
20	1e-08	000	–	0.00	8.96	19.999	4.43	4.05	1.92	0.262	8.52e-3	1.20
20	1e-08	300	0.18	0.28	9.98	19.999	6.17	5.18	2.21	0.381	1.20e-4	1.96
20	1e-08	600	0.33	0.55	10.6	19.952	4.83	4.36	2.00	0.823	5.90e-2	1.35
40	1e-08	700	1.15	0.55	5.77	35.795	13.5	12.8	4.04	1.79	1.87e-1	5.94
60	1e-08	800	2.41	0.57	4.55	48.975	25.6	24.0	7.38	3.58	4.14e-2	12.8
85	1e-08	800	4.15	0.53	3.86	19.868	19.9	18.8	5.79	7.89	1.75e+0	12.3

with 300 km s^{-1} ($J_{\rm tot} = 3.6\,10^{52}$ erg s). So a velocity of 600 km s^{-1}, which at first sight seems extremely fast, is probably the average velocity at Z=10^{-8}. In the second series of models, I follow the exploratory work of Meynet et al. [11] and compute models at Z=10^{-8} with initial masses of 40, 60 and 85 $M_\odot$ and initial rotational velocities of 700, 800 and 800 km s^{-1} respectively. Note that, for these models as well, the initial total angular momentum is similar to the one contained in solar metallicity models with rotational velocities of 300 km s^{-1}. Since this is the case, velocities between 600 and 800 km s^{-1} are considered in this work as the average rotational velocities at these very low metallicities.

EVOLUTION OF THE 20 $M_\odot$ MODELS

Mass loss becomes gradually unimportant as the metallicity decreases in the 20 $M_\odot$ models. At solar metallicity, the rotating 20 $M_\odot$ model loses more than half of its mass and at $Z = 10^{-8}$ less than 0.3% (see Table 1). This means that at very low metallicities, the dominant effect of rotation is mixing for the mass range around 20 $M_\odot$. The impact of rotational mixing is best pictured in the Kippenhahn diagram (see Fig. 1). During hydrogen burning and the start of helium burning, mixing increases the core sizes. Mixing of helium above the core suppresses the intermediate convective zones linked to shell H–burning. So far the impact of mixing at $Z = 10^{-8}$ is the same as at higher metallicities. However, after some time in He–burning, the mixing of primary carbon and oxygen into the H–burning shell is important enough to boost significantly the strength of the shell. As a result, the size of the helium burning core becomes and remains smaller than in the non–rotating model. The yield of ^{16}O being closely correlated with the size of the CO core, it is therefore reduced due to the strong mixing. At the same time carbon yields are increased. This produces an upturn of C/O at very low metallicities.

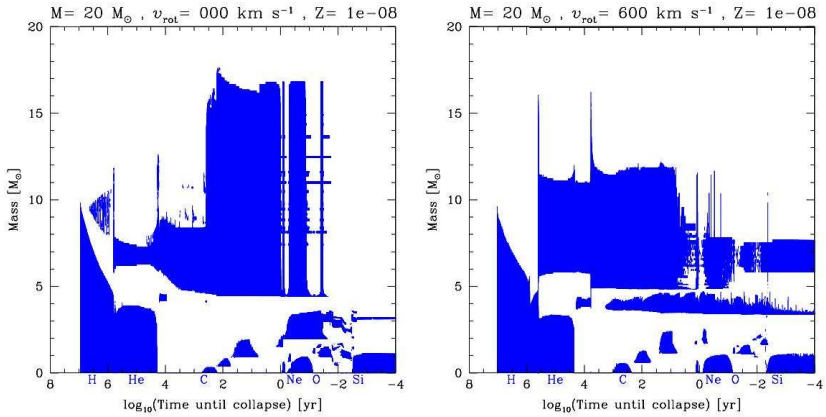

FIGURE 1. Kippenhahn diagrams of $20M_{\odot}$ models at $Z = 10^{-8}$ with $\upsilon_{\rm ini} = 0\,{\rm km\,s^{-1}}$ (*left*) and $600\,{\rm km\,s^{-1}}$ (*right*).

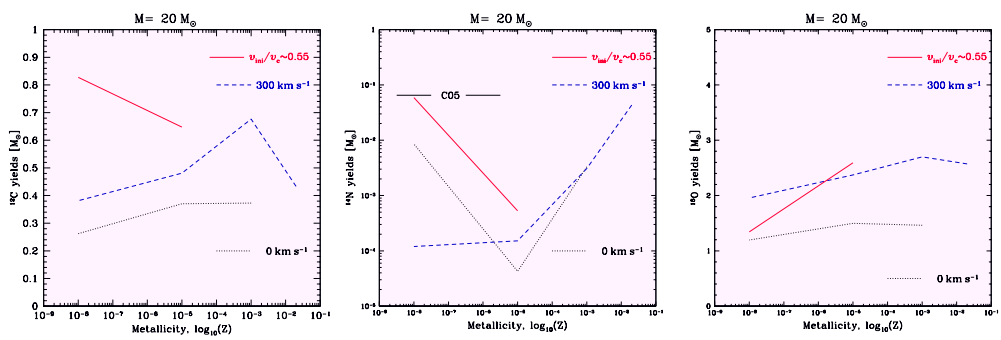

FIGURE 2. Stellar yields of ^{12}C (*left*), ^{14}N (*center*) and ^{16}O (*right*) as a function of the initial metallicity of the models. The solid red, dashed blue and dotted black lines represent respectively the models with $\upsilon_{\rm ini}/\upsilon_c \sim 0.55$ ($\upsilon_{\rm ini}$=500 km s^{-1} at $Z = 10^{-5}$ and $\upsilon_{\rm ini}$=600 km s^{-1} at $Z = 10^{-8}$), with $\upsilon_{\rm ini}$=300 km s^{-1} and without rotation. For nitrogen, the horizontal mark with C05 in the middle corresponds to the value deduced from the chemical evolution models of Chiappini et al. [4].

Stellar yields of CNO elements

The yields of ^{12}C, ^{14}N and ^{16}O are presented in Fig. 2 and their numerical values are given in Table 1 [see 16, for more details]. The most stringent observational constraint at very low Z is a very high primary ^{14}N production [4, 6], of the order of 0.06 $M_{\odot}$ per star. In Fig. 2 (*center*), we can see that only the model at $Z = 10^{-8}$ and with $\upsilon_{\rm ini}$=600 km s^{-1} can reach such high values. The bulk of ^{14}N is produced in the convective zone created by shell hydrogen burning (see Fig. 1 *right*). If this convective zone deepens enough to engulf carbon (and oxygen) rich layers, then significant amounts of primary ^{14}N can be produced ($\sim$0.01$M_{\odot}$). This occurs in both the non–rotating model and the fast rotating model but for different reasons. In the non–rotating model, it occurs due to structure rearrangements similar to the third dredge–up at the end of carbon burning. In the model with $\upsilon_{\rm ini}$ =600 km s^{-1} it occurs during shell helium burning because of the strong mixing of carbon and oxygen into the hydrogen shell burning zone.

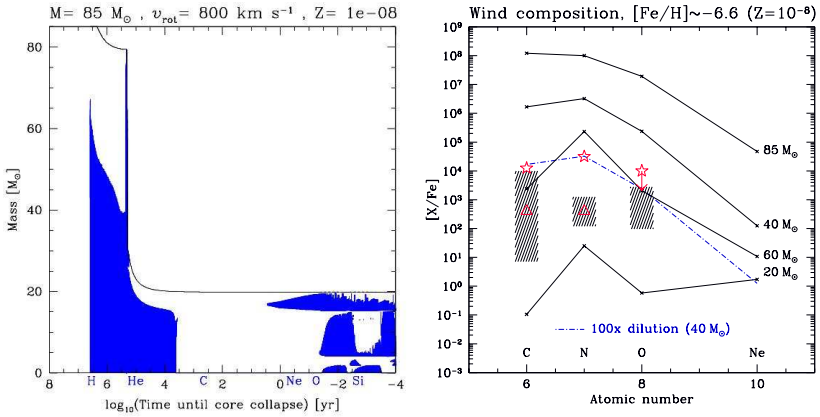

FIGURE 3. *Left*: Kippenhahn diagrams of the 85 $M_\odot$ model at $Z = 10^{-8}$ with $\upsilon_{\rm ini} = 800\,{\rm km\,s^{-1}}$. *Right*: The solid lines represent the chemical composition of the wind material of the of the different models at $Z = 10^{-8}$. The hatched areas correspond to the range of values measured at the surface of giant CEMP stars: HE 0107-5240, [Fe/H]$\simeq$ -5.3 [10]; CS 22949-037, [Fe/H]$\simeq$ -4.0 [19, 20]; CS 29498-043, [Fe/H]$\simeq$ -3.5 [21]. The empty triangles [22]([Fe/H]$\simeq -4.0$) and stars [8] ([Fe/H]$\simeq -5.4$, only an upper limit is given for [O/Fe]) correspond to non-evolved CEMP stars.

TABLE 2. Initial mass (1), metallicity (2) and rotation velocity [km s^{-1}] (3) and stellar wind ejected masses [$M_\odot$] for carbon (4), nitrogen (5) and oxygen (6).

$M_{\rm ini}$	$Z_{\rm ini}$	$\upsilon_{\rm ini}$	^{12}C	^{14}N	^{16}O
20	1e-08	600	3.44e-12	3.19e-10	6.69e-11
40	1e-08	700	5.34e-03	3.63e-03	2.42e-03
60	1e-08	800	1.80e-05	6.87e-04	5.49e-05
85	1e-08	800	6.34e+00	1.75e+00	3.02e+00

Models with higher initial masses at $Z = 10^{-8}$ also produce large quantities of primary nitrogen. More computations are necessary to see over which metallicity range the large primary production takes place and to see whether the scatter in yields of the models with different masses and metallicities is compatible with the observed scatter.

EVOLUTION OF THE MODELS AT $Z = 10^{-8}$

Contrarily to what was initially expected from very low metallicity stars, mass loss can occur in massive stars [11]. The mass loss occurs in two phases. The first phase is when the star reaches break–up velocities towards the end of the main sequence. Due to this effect stars, even metal free ones, are expected to lose about 10% of their initial masses for an average initial rotation. The second phase in which large mass loss can occur is during the RSG stage. Indeed, stars more massive than about 60 $M_\odot$ at $Z = 10^{-8}$ become RSG and dredge–up CNO elements to the surface. This brings the total metallicity of the surface to values within an order of magnitude of solar and triggers large mass loss. The final masses of the models are given in Table 1. The case of the 85 $M_\odot$ model is

extremely interesting (see Fig. 3 *left*) since it loses more than three quarter of its initial mass. It even becomes a WO star.

Wind composition and CRUMPS stars

In Fig. 3 (*right*), we compare the chemical composition of the wind material with abundances observed in non-evolved carbon rich extremely and ultra [8] metal poor stars. The ejected masses of the wind material are also given in Table 2. It is very interesting to see that the wind material can reproduce the observed abundance in two ways. Either, the wind material is richer than necessary and dilution (by a factor 100 for example for the 40 $M_\odot$ models and HE1327-2326) with the ISM is needed or the wind has the right enrichment (for example the 60 $M_\odot$ and HE1327-2326) and the low mass star could form from pure wind material. The advantage of the pure wind material is that it has a ratio $^{12}C/^{13}C$ around 5 [11] and it can explain Li depletion. With or without dilution, the wind material has the advantage that it brings the initial metallicity of the low mass star above the critical value for its formation [23].

ACKNOWLEDGMENTS

I would like to thank warmly the organisation and Prof. Nomoto and his group for the financial support and the kind hospitality.

REFERENCES

1. R. Cayrel, E. Depagne, M. Spite, et al., *A&A* **416**, 1117–1138 (2004).
2. M. Spite, R. Cayrel, B. Plez, et al., *A&A* **430**, 655–668 (2005).
3. G. Israelian, A. Ecuvillon, R. Rebolo, et al., *A&A* **421**, 649–658 (2004).
4. C. Chiappini, F. Matteucci, and S. K. Ballero, *A&A* **437**, 429–436 (2005).
5. P. François, F. Matteucci, R. Cayrel, et al., *A&A* **421**, 613–621 (2004).
6. N. Prantzos, *astro-ph/0411392, NIC8* (2004), `arXiv:astro-ph/0411392`.
7. S. G. Ryan, W. Aoki, J. E. Norris, and T. C. Beers, *ApJ, in press* (2005), `astro-ph/0508475`.
8. A. Frebel, W. Aoki, N. Christlieb, et al., *Nature* **434**, 871–873 (2005).
9. W. Aoki, A. Frebel, N. Christlieb, et al., (2005), `arXiv:astro-ph/0509206`.
10. N. Christlieb, B. Gustafsson, A. J. Korn, et al., *ApJ* **603**, 708–728 (2004).
11. G. Meynet, S. Ekström, and A. Maeder, *A&A accepted* (2005), astro-ph/0510560.
12. R. Hirschi, G. Meynet, and A. Maeder, *A&A* **425**, 649–670 (2004).
13. C. A. Iglesias, and F. J. Rogers, *ApJ* **464**, 943–+ (1996).
14. J. S. Vink, and A. de Koter, (2005), `arXiv:astro-ph/0507352`.
15. R. Hirschi, G. Meynet, and A. Maeder, *A&A* **433**, 1013–1022 (2005).
16. R. Hirschi, *A&A, in prep* (2006).
17. I. Fukuda, *PASP* **94**, 271–284 (1982).
18. T. Abel, G. L. Bryan, and M. L. Norman, *Science* **295**, 93–98 (2002).
19. J. E. Norris, S. G. Ryan, and T. C. Beers, *ApJ* **561**, 1034–1059 (2001).
20. E. Depagne, V. Hill, M. Spite, et al., *A&A* **390**, 187–198 (2002).
21. W. Aoki, J. E. Norris, S. G. Ryan, et al., *ApJ* **608**, 971–977 (2004).
22. B. Plez, and J. G. Cohen, *A&A* **434**, 1117–1124 (2005).
23. V. Bromm, (2005), `arXiv:astro-ph/0509354`.